To be published in Photonics Research:

Title: Self-consistent Maxwell-Bloch model for high-order harmonic generation in nanostructured semiconductors

Authors: Anton Rudenko,Maria Hagen,Jorg Hader,Stephan Koch,Jerome Moloney

Accepted: 05 July 22

Posted 06 July 22

DOI: https://doi.org/10.1364/PRJ.463258

Self-consistent Maxwell-Bloch model for high-order harmonic generation in nanostructured semiconductors

ANTON RUDENKO,[1,*] MARIA K. HAGEN,[2] JÖRG HADER,[1] STEPHAN W. KOCH,[1,2] AND JEROME V. MOLONEY[1]

[1]*Arizona Center for Mathematical Sciences and Wyant College of Optical Sciences, University of Arizona, Tucson, Arizona 85721, USA*
[2]*Department of Physics and Material Sciences Center, Philipps-Universität Marburg, Renthof 5, Marburg 35032, Germany*
[*]*antmipt@gmail.com*

Abstract: In pursuit of efficient high-order harmonic conversion in semiconductor devices, modeling insights into the complex interplay between ultrafast microscopic electron-hole dynamics, nonlinear pulse propagation, and field confinement in nanostructured materials are urgently needed. Here, a self-consistent approach coupling semiconductor Bloch and Maxwell equations is applied to compute transmission and reflection high-order harmonic spectra for a finite slab and sub-wavelength nanoparticle geometries. An increase of the generated high harmonics by several orders of magnitude is predicted for gallium arsenide nanoparticles with a size maximizing the magnetic dipole resonance. Serving as a conceptual and predictive tool for ultrafast spatio-temporal nonlinear optical response of nanostructures with arbitrary geometry, our approach is anticipated to deliver new strategies for optimal harmonic manipulation in semiconductor metadevices.

1. Introduction

All-dielectric nanostructured materials have been extensively applied to enhance and to confine the electric and magnetic fields at subwavelength scales for nonlinear optical applications [1–4]. Several strategies were proposed to increase the second- and third-order nonlinear conversion efficiency in semiconductors, based on Mie resonances in high refractive index nanostructures [5, 6], as well as resonant metasurfaces [7–9]. Recently, a new paradigm of harmonic generation beyond the perturbative regime by strong field excitation has been demonstrated in semiconductors, opening new frontiers for previously non-accessible enhanced high-order harmonic spectra, consisting of odd and even harmonics and stretching far beyond third-order nonlinearities [10–15], and ultrafast all-optical modulation [16–19]. Comprehensive understanding of these coherent non-linear excitation processes in semiconductors is still lacking and self-consistent models are highly challenging due to the inclusion of the dynamical material response on a quantum level beyond the perturbative regime. The nonlinear conversion efficiency strongly depends on multiple involved phenomena such as intra-band and inter-band excitation dynamics [10,11,17], absorption induced by free carriers limiting the harmonics yield above the material bandgap [7] and shifting the nanostructure resonance positions [4, 20], and nonlinear propagation effects [21, 22].

The nature of odd and even harmonic generation in semiconductors has been established only recently, underlying the pronounced role of quantum interference and indirect transitions between the valence and the conduction bands [11, 23, 24]. The latter effects can be described by a quantum approach, as provided by the semiconductor Bloch equations (SBE) under inclusion of more than two mutually dipole coupled bands [25]. This momentum-resolved approach evaluates microscopic coherent carrier densities and polarizations within the non-equilibrium

electronic system, considering the full Brillouin zone. Typically a realistic model for the electronic band structure for a particular semiconductor is provided by density functional theory (DFT) simulations. In contrast to the perturbative models, the SBE automatically include nonlinearities of any order as well as the full dynamic evolution of the electronic material excitations. Furthermore, the non-perturbative nonlinearities were shown to play a significant role in off-resonant strong-field excitation and high harmonic generation in semiconductors, attributed to dynamic intra-band oscillations which can only be captured by employing a dynamic microscopic model like SBE [26, 27]. These non-perturbative scaling laws for high harmonics are influential in GaAs for laser intensities of at least 1 GW/cm^2 [21, 26] and can lead to an increase in the high-harmonic yield.

In order to simulate the nonlinear spectrum evolution upon ultrashort laser pulse propagation through bulk material, the SBE were further coupled to unidirectional or 1D/2D propagation codes by macroscopic polarization currents [22, 28, 29]. Up to date, only few works have focused on the self-consistent coupling between full-vector Maxwell equations and SBE [30–32], albeit not for harmonic generation. A 3D modeling is essential here not only to reproduce the exact geometry and resonant nature of the nanostructures, but also to take account for inhomogeneous distribution of laser-induced carriers [17, 18, 33, 34].

In the current work, we demonstrate the feasibility and robustness of a coupled Maxwell-Bloch approach for investigating the high-order harmonic spectra for a finite slab and 3D sub-wavelength nanoparticle geometries in the non-perturbative regime of ultrashort laser pulse excitation. Driven either by a Fabry-Perot-like standing wave resonator or by magnetic dipole resonances, inhomogeneously photo-induced carriers are localized in the semiconductor material, producing enhanced even and odd harmonics.

2. Numerical model

The approach consists of two coupled parts: Maxwell equations with nonlinear polarization $\vec{P}$ and current $\vec{J}$ sources responsible for inter-band and intra-band excitations respectively and the dynamic SBE, here utilizing a three-band structure model of a direct-gap non-centrosymmetric semiconductor using material parameters representative for gallium arsenide (GaAs). The SBE are sourced by the electric field $\vec{E}$ providing the non-perturbative materials response in form of a macroscopic polarization and current for Maxwell input. The SBE are solved in each spatial point of the nonlinear material.

2.1. Propagation

The propagation model is based on full-vector Maxwell equations with the macroscopic currents to include linear dispersion, inter-band and intra-band excitation upon ultrashort pulse excitation as follows

$$\begin{cases} \dfrac{\partial \vec{E}}{\partial t} = \dfrac{\nabla \times \vec{H}}{\epsilon_0 \epsilon_b} - \dfrac{\left[\sum\limits_i \vec{J_{disp_i}} + \vec{J} + \dfrac{\partial \vec{P}}{\partial t}\right]}{\epsilon_0 \epsilon_b} \\ \dfrac{\partial \vec{H}}{\partial t} = -\dfrac{\nabla \times \vec{E}}{\mu_0}, \end{cases} \tag{1}$$

where $\vec{E}$ and $\vec{H}$ are the electric and the magnetic fields, ϵ_0 and μ_0 are the permittivity and the permeability of free space, and ϵ_b is the background dielectric constant. The dispersion relation for our GaAs model is applied from Ref. [35] through the current $\vec{J_{disp_i}}$ in Eq. (1). $\vec{J}$ and $\frac{\partial \vec{P}}{\partial t}$ correspond to inter- and intra-band currents respectively.

Throughout the paper, a linearly polarized plane wave excitation source is used. The electric field source is chosen to be an x-polarized Gaussian pulse with a full width at half maximum

of $\theta = 100$ fs. Light propagates along the Z direction. Maxwell equations are solved by finite-difference time-domain (FDTD) approach with convolutional perfect matched layers (CPML) at the boundaries [36]. For the 1D problem, a spatial step of 10 nm and a temporal step of ≈ 2 as were chosen. For the 3D problem, the corresponding resolution was 5 nm spatially and ≈ 4 as temporally. Generally, temporal steps smaller than the ones defined by the Courant-Friedrichs-Lewy condition were required to resolve high-order harmonics.

2.2. Electronic band structure

Our GaAs band structure parameters are obtained via density functional theory (DFT) assuming (111) crystal orientation. In our simulations, we include the mutually dipole coupled conduction e, split-off valence h_1 and light hole valence bands h_2. The dipole coupling strength $d_{ll'}$ for the corresponding electronic transitions ll' and energy dispersion of each band ϵ_l, shown in Fig. 1(a, b), are derived as a fit to the results of our DFT calculation using the Vienna ab-initio simulation package [37, 38]. The accurate reproduction of the band gap is realized by employing the Heyd-Scuseria-Ernzerhof hybrid functional [39] customized for GaAs. In order to keep our evaluations as simple as possible, we neglect the dipole phases and Berry phases which is an acceptable approximation for the chosen excitation conditions [24]. We use a momentum grid size $[-k_{max}; k_{max}]$ with 1200 points where $k_{max} = \sqrt{3}\pi/a$ and $a = 5.663$ Å is the lattice constant, respectively. Our consideration of a single path through the Brillouin zone (BZ) along Γ-L direction is justified by the use of a linearly polarized source along this direction. In order to avoid nonphysical reflections at the boundaries of the BZ, a third-order polynomial fit is applied to the energy boundary points, in order to conserve both the energy values and their derivatives. The resulting energy gradients $\nabla_k \epsilon_l$ are shown in Fig. 1(c), smoothly decaying to zero at the edges of the grid.

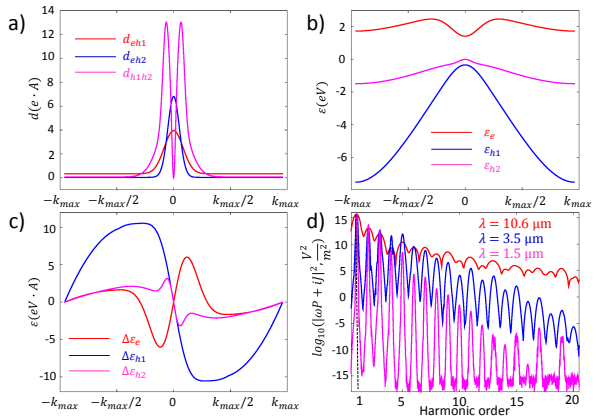

Fig. 1. (a-c) Three-band structure for a non-centrosymmetric direct-gap semiconductor: GaAs (111) inspired (a) dipole coupling strength, (b) energies and (c) their gradients. (d) High-harmonic spectra generated by a SBE model for $E = 10^8$ V/m, $\theta = 100$ fs FWHM pulse duration and long-, mid- and near-infrared wavelengths λ.

2.3. Semiconductor Bloch equations (SBE)

The macroscopic intra-band current and inter-band polarization are calculated through complex microscopic polarizations $p_k^{ll'}$ and carrier distributions f_k^l as follows

$$\begin{cases} P_x = \sum\limits_{k,l,l'} d_k^{ll'} Re(p_k^{ll'}) \\ J_x = \dfrac{e}{\hbar} \sum\limits_{k,l} \left(\nabla_k \varepsilon_k^l\right) f_k^l, \end{cases} \tag{2}$$

where l, l' stand for the electron e or hole h_1, h_2 bands and the summation is performed for all momentum points k. The SBE with a sourced linearly x-polarized electric field [25] are solved in order to define the microscopic polarizations and carrier densities as follows

$$\begin{cases} i\hbar \frac{\partial}{\partial t} p_k^{h_i e} = (\varepsilon_k^e + \varepsilon_k^{h_i} + ieE_x(t)\nabla_k - i\hbar/T_2) p_k^{h_i e} \\ + \left[d_k^{h_j h_i} p_k^{h_j e} - d_k^{e h_j} p_k^{h_i h_j} - d_k^{e h_i} (1 - f_k^e - f_k^{h_i}) \right] E_x(t) \\ i\hbar \frac{\partial}{\partial t} p_k^{h_1 h_2} = (\varepsilon_k^{h_1} - \varepsilon_k^{h_2} + ieE_x(t)\nabla_k - i\hbar/T_2) p_k^{h_1 h_2} \\ + \left[d_k^{e h_1} p_k^{e h_2} - d_k^{h_2 e} p_k^{h_1 e} + d_k^{h_2 h_1} (f_k^{h_1} - f_k^{h_2}) \right] E_x(t) \\ \hbar \frac{\partial}{\partial t} f_k^e = -2E_x(t) \sum\limits_i \left[Im(d_k^{e h_i} p_k^{e h_i}) \right] + eE_x(t)\nabla_k f_k^e \\ \hbar \frac{\partial}{\partial t} f_k^{h_i} = -2E_x(t) \left[Im(d_k^{h_j h_i} p_k^{h_j h_i}) + Im(d_k^{e h_i} p_k^{e h_i}) \right] + eE_x(t)\nabla_k f_k^{h_i}, \end{cases} \tag{3}$$

where $i = 1, 2$, $j \neq i$ and $T_2 = 20$ fs is the dephasing time, and $Re()$ and $Im()$ stand for the real and the imaginary parts of the microscopic polarization, respectively. Since the Coulomb interaction was shown to only play a minor role for off-resonant strong field excitation, it is sufficient for the present purposes to include it only via the dephasing term [11]. The microscopic carriers in the conduction band are summed up and averaged through $N = 1200$ momentum points as follows $N_e = \sum_k^N f_k^e / N$.

In order to solve the SBE, a fourth-order Runge-Kutta method is applied for the ensemble of microscopic polarizations $p_k^{ll'}$ and carrier distributions f_k^l. The macroscopic quantities P_x and J_x are then evaluated according to Eq. (2) after each four-step procedure. A fully symmetric fourth-order finite-difference approximation is implemented for the microscopic gradient values $\nabla_k p_k^{ll'}$ and $\nabla_k f_k^l$. Periodic boundary conditions are then applied for the microscopic polarizations and distributions at the borders of the BZ. For an uncoupled SBE model, the electric field is sourced directly to the SBE and the Fourier transforms of the local emission spectra $|iJ_x + P_x\omega|^2$ are plotted for the laser wavelengths of interest in Fig. 1(d). The results with $N = 1200$ momentum points have been tested for convergence, giving identical results for the larger number of points $N = 2400$. The local emission spectra indicate a complex behavior for high-order odd and even harmonics. The odd harmonics are mainly the consequence of direct transitions from the valence to conduction band, which can be illustrated by a perturbative expansion of the contributions to the materials response from the SBE. Eq. (3) for microscopic polarizations gives rise to odd-order terms which involve only the coupling between two bands $d_k^{h_i e}(1 - f_k^e - f_k^{h_i}) E_x \propto d^{h_i e} E + d^{h_i e^3} E^3 + ...$, whereas the even order contributions appear in mixed terms of the expansion $(d_k^{h_i h_j} p_k^{h_j e} - d_k^{h_j e} p_k^{h_i h_j}) E_x \propto d^{h_i h_j} d^{h_j e} E^2 + (d^{h_i h_j} d^{h_j e})^2 E^4 + ...$, which show a coupling of three bands and can be attributed to indirect transition pathways. As a result, at least a three-band structure is required to fully describe both even and odd harmonics in our model.

In the framework of the SBE model, the major changes in both real and imaginary refractive index are considered via the complex intra-band and inter-band currents. Band-filling dynamics is included via the Pauli blocking factor $(1 - f_k^e - f_k^h)$, which reduces the oscillation strength as

the plasma density increases. Complementary contributions might be expected by the bandgap shrinkage due to carrier-carrier scattering in Coulomb interactions which are not included in the current model and could be further incorporated in the semiconductor Bloch formalism as proposed in Ref. [25]. It was shown in that Reference that for the strongly off-resonant excitation Coulomb effects do not lead to additional features, but only influence spectral details and do so only in materials with exceptionally high Coulomb interaction like monolayer TMDCs. For the GaAs system investigated here, Coulomb-induced renormalizations are almost two orders of magnitude smaller than in the TMDCs and should be of minor importance. Including Coulomb effects would dramatically increase the numerical effort. Therefore, we only include the Coulomb scattering effects through the polarization dephasing term but neglect the bandgap and field renormalization.

2.4. Coupling Maxwell equations & SBE

Our numerical method for the coupled Maxwell equations (1) and SBE (3) evaluates additionally the nonlinear electric field component E_x inside a fourth-order Runge-Kutta procedure applied for the microscopic polarization and carrier densities. The macroscopic quantities at each spatial position affect the carrier dynamics and the nonlinear propagation at each subsequent temporal step. Our computing algorithm uses spatially parallel implementation based on graphics processing units (GPU).

The field is sourced in vacuum at a distance from the nonlinear material. The time history of the electric field evolution is recorded in space positions before and after hitting the semiconductor material to obtain separate reflected and transmission field signals, which are then further analyzed by Fourier transforms. A harmonic and decaying window function is applied at the boundaries of the temporal domain [35] in order to reduce the noise floor due to the finite size of the used Gaussian pulse and the accumulation effects related to the numerical dispersion.

3. Results and discussion

For our study, there are two specific regimes of interest for harmonic generation in semiconductor nanomaterials: a propagative regime in finite structures on the distances of order or larger than laser wavelength and a field confinement regime in subwavelength nanostructures, where the field can be significantly enhanced and the photo-generated carriers are localized inside the nanostructure.

3.1. Propagation in a finite slab: Fabry-Perot resonances

Firstly, we investigate the ultrashort laser pulse propagation through finite slabs of different thicknesses, effectively representing examples of a Fabry-Perot resonator due to the refractive index differences between vacuum and semiconductor material. Light waves entering the slab, being smaller than the optical pulse length $d < c\theta \approx 30\mu m$, undergo multiple partial reflections, constructively interfering at the resonant frequency. Apart from creating multiple transmitted sub-pulses, nonlinear propagation is accompanied by the generation of electron densities and absorption losses upon propagation. For our study, ultrashort pulse with a fundamental $\lambda = 10.6\mu m$ wavelength is chosen exhibiting a pronounced interplay of direct and indirect inter-band transitions contributing to high-order harmonic generation.

The spatio-temporal evolution of the electric fields for slab thicknesses of $12\mu m$ and $24\mu m$ is shown in Fig. 2(a, c) with the laser pulse propagating from down upwards. We see that for the thicker slab, the first and secondary reflection signals are separated in time, whereas for the thinner slab, they overlap. The maximum electron density distributions established at the end of the pulse are detailed in Fig. 2(b, d), representing periodic concentrated regions of increased charge carriers spaced by $\lambda/n \approx 3.1\mu m$, created by standing waves as a result of an interference between the transmitted and reflected waves from the slab boundaries ($t > 1$ ps). Strong spatial

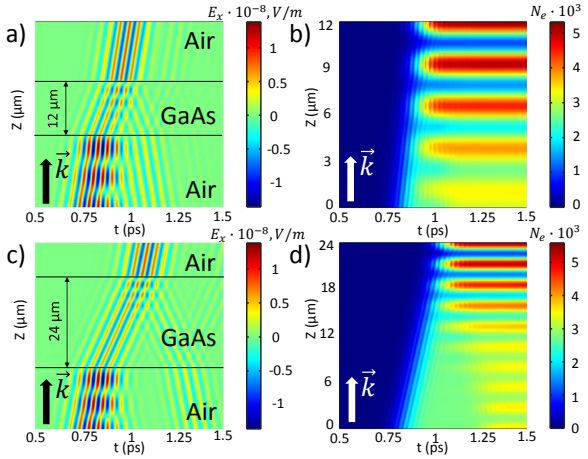

Fig. 2. Spatio-temporal evolution of (a, c) the electric fields, (b, d) averaged carrier densities inside the slab of (a, b) $12\mu m$ and (c, d) $24\mu m$ thicknesses. Laser irradiation parameters are $E = 10^8$ V/m, $\theta = 100$ fs FWHM pulse duration and $\lambda = 10.6\mu m$. $\vec{k}$ indicates the propagation direction of laser pulse. Solid lines in (a, c) show the position of the slab.

density gradients are formed on the back side of the slab, potentially contributing to an enhanced harmonic yield.

In Fig. 3(a), we show spectra of the transmitted fields as a function of the propagation distance in comparison to the local emission spectrum $|iJ_x + P_x\omega|^2$ obtained by the uncoupled SBE model. Here, we refer to the uncoupled point SBE model by indicating that the electric field is sourced by a plane wave source inside the material without solving Maxwell equations, i. e. excluding propagation effects. We note that the harmonic yield tends to increase for a larger slab thickness, keeping approximately a similar shape as the spectrum of the point model. In addition, the appearance of the sub-harmonics is also apparent between 6th and 7th harmonics attributed to frequency mixing in nonlinear propagation, as well non-trivial behavior for higher-order harmonics with increasing propagation distance.

Reflection and transmission spectra are compared for $12\mu m$ and $48\mu m$ slabs in Fig. 3(b-e) (Fourier Transforms in (b, c) and the corresponding temporal signals in (d, e)).

3.2. Subwavelength nanoparticle: excitation of Mie resonances

Nonlinear field effects can be significantly enhanced in subwavelength nanostructures of high refractive index materials supporting Mie resonances. We investigate here the ultrashort laser pulse excitation of a single spherical GaAs-like nanoparticle at $\lambda = 1.5\mu m$ near-infrared wavelength (refractive index $n = 3.3817$, transparency range). In this excitation regime, the harmonics starting from the second lie above the material bandgap ($E_g = 1.42$ eV). Nevertheless, as the considered subwavelength radii in the range $150 - 240$ nm are much smaller than the attenuation length of the photo-induced free carriers, the generated harmonics can be efficiently extracted, even if lying within the absorption region.

Extinction cross-sections as a function of the nanoparticle radii at $1.5\mu m$ wavelength are calculated by Mie theory [40] and plotted in Fig. 4(a). The sizes of choice are marked by colored points, corresponding to different positions respective to a magnetic dipole resonance (MD) and contrasting electric field distributions inside the nanoparticles. The intensities corresponding to an incident field $E = 10^8$ V/m are plotted in Fig. 4(c-f) for the sizes of 150 nm, 180 nm, 210 nm and 240 nm, respectively. For the smallest nanoparticle within the Rayleigh range, the

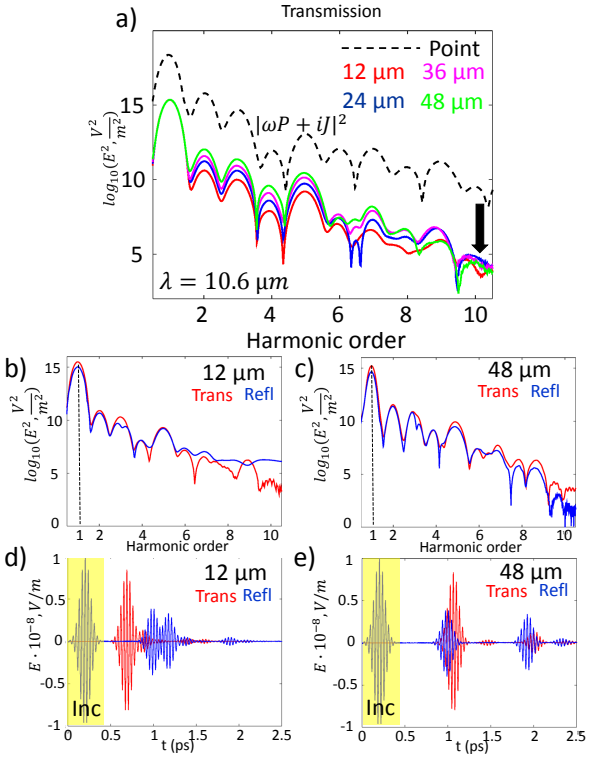

Fig. 3. (a) Transmission spectra (solid lines) upon propagation on distances $12, 24, 36, 48\mu m$ compared to the emission spectra from point SBE model (dashed line). Comparison of transmission (red) and reflection (blue) spectra for slabs of (b) $12\mu m$ and (c) $48\mu m$ thickness, temporal evolution of the corresponding electric fields for (d) $12\mu m$- and (e) $48\mu m$-slabs. Incident pulses are marked by yellow boxes. Laser irradiation parameters are $E = 10^8$ V/m, $\theta = 100$ fs FWHM pulse duration and $\lambda = 10.6\mu m$.

fields inside the material are weak and almost homogeneous. In contrast, larger sizes exhibit toroidal field distribution with the strongest field enhancement for the radius 210 nm close to the magnetic dipole resonance. With increasing size, the intensity decreases following the extinction cross-section. The resulting 1D spatial carrier distributions along the propagation direction (from left to right) are compared for different radii in Fig. 4(b). The highest values and inhomogeneity of charge densities are obtained for the nanoparticle of 210 nm radius.

Figure 5(a, b) shows the computed transmission and reflection spectra for the nanoparticles of different radii, indicating the excitation of second, third and fourth-order harmonics. The field spectra are collected at $(0, 0, 1)\mu m$ and $(0, 0, -1)\mu m$ respectively at $1\mu m$ distance from the nanoparticle center along the propagation axis Z. The harmonic yield for the nanoparticle $R = 210$ nm close to the magnetic dipole resonance exceeds by several orders of magnitude the results for off-resonant particles of smaller sizes $R = 150$ nm and $R = 180$ nm, as well as at least by two orders the nonlinear efficiency of third and fourth-order harmonics for a larger nanoparticle of $R = 240$ nm, close to an electric dipole resonance.

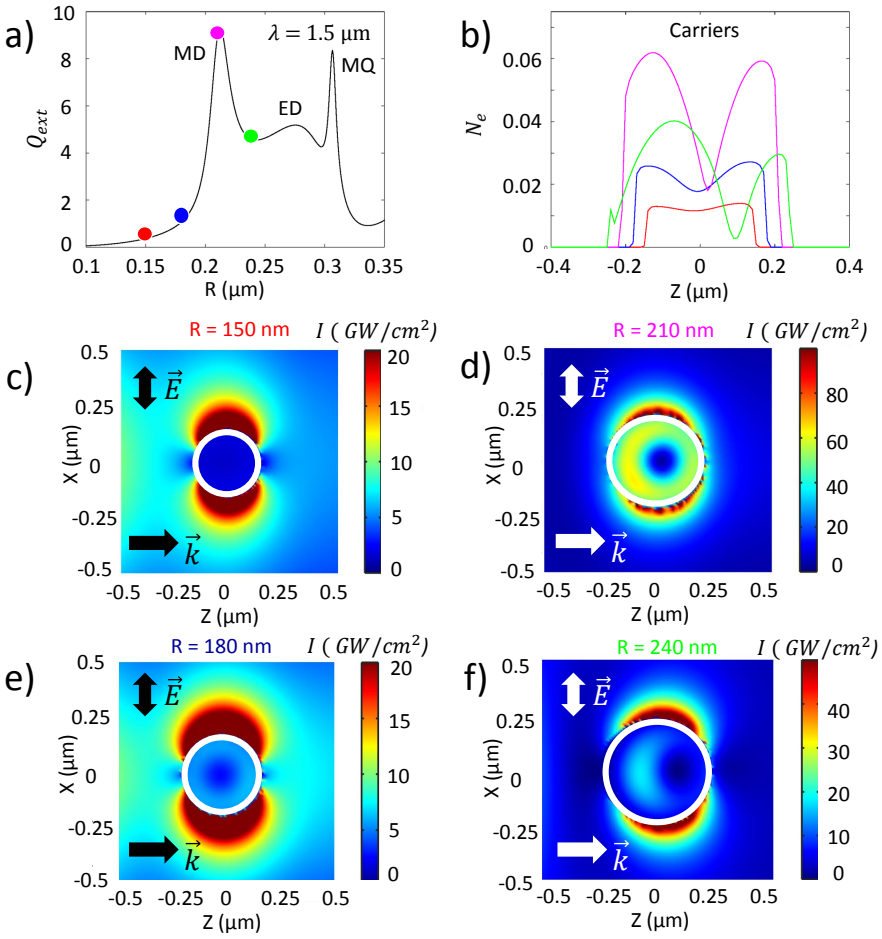

Fig. 4. (a) Extinction cross-section for GaAs nanoparticles of different radii. (b) 1D conduction band densities N_e at the distance from the nanoparticle center 0 along the propagation direction z, (c-f) averaged intensity distributions in the propagation plane (2D) for GaAs nanoparticles excited by $E = 10^8$ V/m incident field at fundamental wavelength $\lambda = 1.5\mu m$. The corresponding radii R are indicated above each sub-figure (c-f) respectively. Laser polarization $\vec{E}$ and propagation direction $\vec{k}$ are shown.

4. Conclusions

In conclusion, we have introduced a microscopic Maxwell-SBE model that allows us to fully analyze high-harmonic generation in semiconductor nanostructures. This approach can be fully customized to accurately model a specific semiconductor material and explicitly consider different crystal orientations and direction dependent effects. Time-dependent carrier dynamics and individual band contributions are fully accessible, allowing us to pinpoint the influences of band structure features. Additionally, phase-dependent effects could be incorporated, including but not limited to the influence of Berry phases for topologically non-trivial materials. The model is also flexible to include different features of the driving field in the analysis, e.g. carrier-envelope phase or even a combination of resonant and off-resonant pulses. This specificity allows for a highly improved quantitative comparison with experimental measurements implying different polarization states without relying on experimental or phenomenological input. The coupled

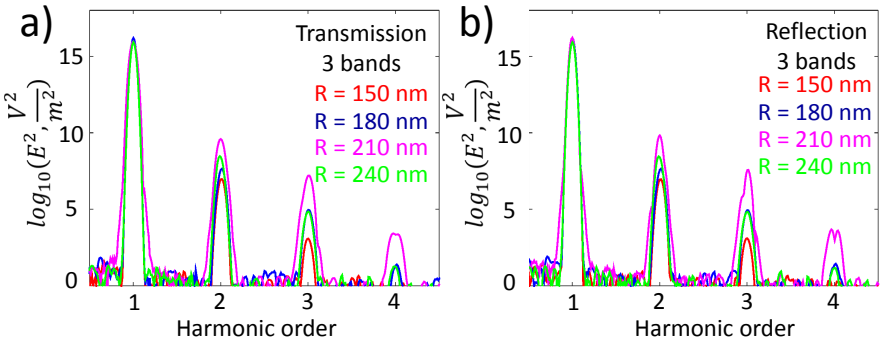

Fig. 5. (a) Transmission and (b) reflection spectra for GaAs nanoparticles of different radii. Laser irradiation parameters are $E = 10^8$ V/m, $\theta = 100$ fs FWHM pulse duration and $\lambda = 1.5\mu m$.

SBE and Maxwell equations approach can be applied to complex geometries and metasurfaces, benefiting from the periodic boundary conditions for the electric and magnetic fields in the Maxwell solver.

We apply our model to the regimes of ultrashort pulse propagation in a finite slab, supporting Fabry-Perot resonances, and in a subwavelength nanoparticle, supporting magnetic dipole Mie resonance. Both regimes are characterized by inhomogeneous carrier distribution inside the structures and generation of even and odd harmonics of a higher yield for the resonant conditions. Overall, implementation of our self-consistent approach to arbitrary geometries has a strong potential for optimal design of semiconductor optical metadevices, with emerging applications for high-resolution imaging and attosecond science.

Funding. This work was supported by an Air Force Office for Scientific Research under awards no. FA9550-19-1-0032 and FA9550-17-1-0246.

Acknowledgments. The authors are grateful to Prof. Miroslav Kolesik for fruitful discussions.

Disclosures. The authors declare no conflicts of interest.

Data availability. Data underlying the results presented in this paper are not publicly available at this time but may be obtained from the authors upon reasonable request.

References

1. A. Krasnok, M. Tymchenko, and A. Alù, "Nonlinear metasurfaces: a paradigm shift in nonlinear optics," Mater. Today **21**, 8–21 (2018).
2. B. Sain, C. Meier, and T. Zentgraf, "Nonlinear optics in all-dielectric nanoantennas and metasurfaces: a review," Adv. Photonics **1**, 024002 (2019).
3. G. Grinblat, "Nonlinear dielectric nanoantennas and metasurfaces: frequency conversion and wavefront control," ACS Photonics **8**, 3406–3432 (2021).
4. V. Zubyuk, L. Carletti, M. Shcherbakov, and S. Kruk, "Resonant dielectric metasurfaces in strong optical fields," APL Mater. **9**, 060701 (2021).
5. D. A. Smirnova, A. B. Khanikaev, L. A. Smirnov, and Y. S. Kivshar, "Multipolar third-harmonic generation driven by optically induced magnetic resonances," ACS Photonics **3**, 1468–1476 (2016).
6. S. V. Makarov, M. I. Petrov, U. Zywietz, V. Milichko, D. Zuev, N. Lopanitsyna, A. Kuksin, I. Mukhin, G. Zograf, E. Ubyivovk *et al.*, "Efficient second-harmonic generation in nanocrystalline silicon nanoparticles," Nano Lett. **17**, 3047–3053 (2017).
7. S. Liu, M. B. Sinclair, S. Saravi, G. A. Keeler, Y. Yang, J. Reno, G. M. Peake, F. Setzpfandt, I. Staude, T. Pertsch *et al.*, "Resonantly enhanced second-harmonic generation using III-V semiconductor all-dielectric metasurfaces," Nano Lett. **16**, 5426–5432 (2016).

8. Z. Liu, J. Wang, B. Chen, Y. Wei, W. Liu, and J. Liu, "Giant enhancement of continuous wave second harmonic generation from few-layer GaSe coupled to high-Q quasi bound states in the continuum," Nano Lett. **21**, 7405–7410 (2021).
9. C. Gigli and G. Leo, "All-dielectric $\chi^{(2)}$ metasurfaces: recent progress," Opto-Electronic Adv. pp. 210093–1 (2022).
10. S. Ghimire and D. A. Reis, "High-harmonic generation from solids," Nat. Phys. **15**, 10–16 (2019).
11. O. Schubert, M. Hohenleutner, F. Langer, B. Urbanek, C. Lange, U. Huttner, D. Golde, T. Meier, M. Kira, S. W. Koch *et al.*, "Sub-cycle control of terahertz high-harmonic generation by dynamical Bloch oscillations," Nat. Photonics **8**, 119–123 (2014).
12. M. Sivis, M. Taucer, G. Vampa, K. Johnston, A. Staudte, A. Y. Naumov, D. Villeneuve, C. Ropers, and P. Corkum, "Tailored semiconductors for high-harmonic optoelectronics," Science **357**, 303–306 (2017).
13. H. Liu, C. Guo, G. Vampa, J. L. Zhang, T. Sarmiento, M. Xiao, P. H. Bucksbaum, J. Vučković, S. Fan, and D. A. Reis, "Enhanced high-harmonic generation from an all-dielectric metasurface," Nat. Phys. **14**, 1006–1010 (2018).
14. M. R. Shcherbakov, H. Zhang, M. Tripepi, G. Sartorello, N. Talisa, A. AlShafey, Z. Fan, J. Twardowski, L. A. Krivitsky, A. I. Kuznetsov *et al.*, "Generation of even and odd high harmonics in resonant metasurfaces using single and multiple ultra-intense laser pulses," Nat. Commun. **12**, 1–6 (2021).
15. G. Zograf, K. Koshelev, A. Zalogina, V. Korolev, R. Hollinger, D.-Y. Choi, M. Zuerch, C. Spielmann, B. Luther-Davies, D. Kartashov *et al.*, "High-harmonic generation from resonant dielectric metasurfaces empowered by bound states in the continuum," ACS Photonics **9**, 567–574 (2022).
16. M. R. Shcherbakov, S. Liu, V. V. Zubyuk, A. Vaskin, P. P. Vabishchevich, G. Keeler, T. Pertsch, T. V. Dolgova, I. Staude, I. Brener *et al.*, "Ultrafast all-optical tuning of direct-gap semiconductor metasurfaces," Nat. Commun. **8**, 1–6 (2017).
17. A. Mazzanti, E. A. A. Pogna, L. Ghirardini, M. Celebrano, A. Schirato, G. Marino, A. Lemaítre, M. Finazzi, C. De Angelis, G. Leo *et al.*, "All-optical modulation with dielectric nanoantennas: Multiresonant control and ultrafast spatial inhomogeneities," Small Sci. **1**, 2000079 (2021).
18. I. S. Sinev, K. Koshelev, Z. Liu, A. Rudenko, K. Ladutenko, A. Shcherbakov, Z. Sadrieva, M. Baranov, T. Itina, J. Liu *et al.*, "Observation of ultrafast self-action effects in quasi-BIC resonant metasurfaces," Nano Lett. **21**, 8848–8855 (2021).
19. E. A. A. Pogna, M. Celebrano, A. Mazzanti, L. Ghirardini, L. Carletti, G. Marino, A. Schirato, D. Viola, P. Laporta, C. De Angelis *et al.*, "Ultrafast, all optically reconfigurable, nonlinear nanoantenna," ACS Nano **15**, 11150–11157 (2021).
20. S. Makarov, S. Kudryashov, I. Mukhin, A. Mozharov, V. Milichko, A. Krasnok, and P. Belov, "Tuning of magnetic optical response in a dielectric nanoparticle by ultrafast photoexcitation of dense electron–hole plasma," Nano Lett. **15**, 6187–6192 (2015).
21. P. Xia, C. Kim, F. Lu, T. Kanai, H. Akiyama, J. Itatani, and N. Ishii, "Nonlinear propagation effects in high harmonic generation in reflection and transmission from gallium arsenide," Opt. Express **26**, 29393–29400 (2018).
22. I. Kilen, M. Kolesik, J. Hader, J. V. Moloney, U. Huttner, M. K. Hagen, and S. W. Koch, "Propagation induced dephasing in semiconductor high-harmonic generation," Phys. Rev. Lett. **125**, 083901 (2020).
23. M. Hohenleutner, F. Langer, O. Schubert, M. Knorr, U. Huttner, S. W. Koch, M. Kira, and R. Huber, "Real-time observation of interfering crystal electrons in high-harmonic generation," Nature **523**, 572–575 (2015).
24. M. K. Hagen and S. W. Koch, "Probing intervalence band coupling via high-harmonic generation in binary zinc-blende semiconductors," physica status solidi (RRL) - Rapid Res. Lett. **15** (2021).
25. U. Huttner, M. Kira, and S. W. Koch, "Ultrahigh off-resonant field effects in semiconductors," Laser & Photonics Rev. **11**, 1700049 (2017).
26. D. Matteo, J. Pigeon, S. Y. Tochitsky, U. Huttner, M. Kira, S. Koch, J. Moloney, and C. Joshi, "Control of the nonlinear response of bulk GaAs induced by long-wavelength infrared pulses," Opt. Express **27**, 30462–30472 (2019).
27. M. Hussain, F. Lima, W. Boutu, H. Merdji, M. Fajardo, and G. O. Williams, "Demonstration of nonperturbative and perturbative third-harmonic generation in MgO by altering the electronic structure," Phys. Rev. A **105**, 053103 (2022).
28. W. Cartar, J. Mørk, and S. Hughes, "Self-consistent Maxwell-Bloch model of quantum-dot photonic-crystal-cavity lasers," Phys. Rev. A **96**, 023859 (2017).
29. J. R. Gulley and D. Huang, "Self-consistent quantum-kinetic theory for interplay between pulsed-laser excitation and nonlinear carrier transport in a quantum-wire array," Opt. Express **27**, 17154–17185 (2019).
30. R. Buschlinger, M. Lorke, and U. Peschel, "Light-matter interaction and lasing in semiconductor nanowires: A combined finite-difference time-domain and semiconductor Bloch equation approach," Phys. Rev. B **91**, 045203 (2015).
31. K. Ravi, Q. Wang, and S.-T. Ho, "A multi-band, multi-level, multi-electron model for efficient FDTD simulations of electromagnetic interactions with semiconductor quantum wells," J. Mod. Opt. **62**, 1158–1182 (2015).
32. C. Jirauschek, M. Riesch, and P. Tzenov, "Optoelectronic device simulations based on macroscopic Maxwell–Bloch equations," Adv. Theory Simulations **2**, 1900018 (2019).
33. A. Rudenko, K. Ladutenko, S. Makarov, and T. E. Itina, "Photogenerated free carrier-induced symmetry breaking in spherical silicon nanoparticle," Adv. Opt. Mater. **6**, 1701153 (2018).
34. J.-K. An and K.-H. Kim, "Efficient non-perturbative high-harmonic generation from nonlinear metasurfaces with low

pump intensity," Opt. & Laser Technol. **135**, 106702 (2021).
35. A. Rudenko, M. K. Hagen, J. Hader, M. Kolesik, S. W. Koch, and J. V. Moloney, "Maxwell-semiconductor Bloch simulations of high-harmonic generation in finite thickness semiconductor slabs," in *Ultrafast Phenomena and Nanophotonics XXVI,* vol. 11999 M. Betz and A. Y. Elezzabi, eds., International Society for Optics and Photonics (SPIE, 2022), pp. 56 – 61.
36. A. Taflove, S. C. Hagness *et al.*, "Computational electrodynamics: the finite-difference time-domain method," Norwood, 2nd Ed. MA: Artech House, l995 (1995).
37. G. Kresse and J. Hafner, "Ab initio molecular-dynamics simulation of the liquid-metal–amorphous-semiconductor transition in germanium," Phys. Rev. B **49**, 14251–14269 (1994).
38. G. Kresse and J. Furthmüller, "Efficiency of ab-initio total energy calculations for metals and semiconductors using a plane-wave basis set," Comput. Mater. Sci. **6**, 15–50 (1996).
39. J. Heyd, J. E. Peralta, G. E. Scuseria, and R. L. Martin, "Energy band gaps and lattice parameters evaluated with the heyd-scuseria-ernzerhof screened hybrid functional," J. Chem. Phys. **123**, 174101 (2005).
40. G. Mie, "Beiträge zur optik trüber medien, speziell kolloidaler metallösungen," Annalen der Physik **330**, 377–445 (1908).